Solar Energy 174 (2018) 1212–1223

Contents lists available at ScienceDirect

Solar Energy

journal homepage: www.elsevier.com/locate/solener

Vacuum enclosures for solar thermal panels Part 1: Fabrication and hot-box testing

Farid Arya[a,*], Roger Moss[b], Trevor Hyde[a], Stan Shire[b], Paul Henshall[c], Philip Eames[d]

[a] Centre for Sustainable Technologies, Ulster University, UK
[b] School of Engineering, University of Warwick, UK
[c] School of Architecture, Oxford Brookes University, UK
[d] Centre for Renewable Energy Systems Technology, Loughborough University, UK

ARTICLE INFO

Keywords:
Vacuum enclosure
Vacuum glazing
Solar absorber
Vacuum insulation
Evacuated flat plate solar collector
Ultrasonic soldering
Hot box calorimeter

ABSTRACT

Non-concentrating solar thermal collectors are generally available in two forms, flat plate or evacuated tube. Recently a third configuration, the evacuated flat plate, has attracted interest due to enhanced performance and aesthetic characteristics. By isolating a solar absorber in a vacuum space (< 1 Pa) heat loss from the absorber can be minimized resulting in improved efficiency. In addition the improved thermal insulation performance of evacuated panels over conventional glazing systems makes them attractive solutions for integration into energy efficient building facades.

This two part paper describes the design, construction techniques and thermal performance of two vacuum enclosures, fabricated at Ulster University, as prototype components for evacuated flat solar collectors. The first enclosure consists of two glass panes sealed to an edge spacer and separated by an array of support pillars on a regular square grid to form a narrow evacuated space. The second enclosure incorporates an uncooled copper sheet to represent a solar thermal absorber. The enclosures were tested at three conditions i.e. with an internal pressure of high vacuum (0.0021 Pa), low vacuum (8.4 Pa) and no vacuum (atmospheric pressure).

Part 1 of this paper describes the fabrication process for the vacuum enclosures and the measurement of their thermal insulation properties using a hot box calorimeter. The theory of heat transfer through an enclosure with support pillars is discussed; experimental results are compared with mathematical models predictions. A fabrication methodology has been successfully established and a U-value of 1.35 $W/m^2 K$ for an enclosure with an internal pressure of 0.0021 Pa has been demonstrated. The experimental results are in good agreement with the predictions.

Part 2 of this paper describes solar simulator testing of the enclosure containing a copper plate. The highest stagnation temperature (121.8 °C) was reached under steady-state conditions in the high vacuum test and was in good agreement with predictions. The transient plate and glass surface temperatures were measured and found to be consistent with the predicted curves.

1. Introduction

Eaton and Blum (1975) proposed a vacuum flat plate (VFP) solar collector in which convective heat losses from an absorber were minimised by placing the absorber in a moderate vacuum (~150–3500 Pa). This raises efficiency especially when operating at high temperatures to supply industrial process heat, when solar insolation is weak or in cold climates. The reduction in heat losses should enable steam production at temperatures of up to 150 °C with efficiencies of nearly 50% (Benz and Beikircher, 1999). Moss et al (2018c) showed that an optimised evacuated flat plate supplying a heating main at 85 °C should deliver twice the annual output of a conventional flat plate collector.

Vacuum flat plate collectors have two advantages over evacuated tube collectors. A larger fraction of the external area is available for heat collection (Beikircher et al., 2015; Henshall et al., 2014) and the slimmer profile enhances architectural appeal. This is important in applications such as the cladding of building façades enabling direct integration into the building envelope. The combination of a solar absorber with a vacuum-insulated glazing can provide solar shading and hot water in summer without unsightly “add-on” solar panels, as well as

* Corresponding author.
E-mail addresses: f.arya@ulster.ac.uk (F. Arya), r.moss@warwick.ac.uk (R. Moss), t.hyde@ulster.ac.uk (T. Hyde), stan.shire@warwick.ac.uk (S. Shire), phenshall@brookes.ac.uk (P. Henshall), p.c.eames@lboro.ac.uk (P. Eames).

https://doi.org/10.1016/j.solener.2018.10.064
Received 19 August 2018; Received in revised form 20 October 2018; Accepted 22 October 2018
Available online 28 October 2018

Nomenclature

a	pillar radius
p	pillar pitch
c	specific heat capacity
d	gap between copper plate and glass
f	conductivity correction factor
h	heat transfer coefficient
k	conductivity
p	pressure
$\dot{q}$	heat flux (W/m^2)
r	radius
t	plate thickness
w	area density (kg/m^2)
z	non-dimensional radius
C	thermal conductance
D	pillar diameter
G	insolation from solar simulator (W/m^2)
G'	dissipation in glass (W/m^2)
H	length of plate (m)
L	pillar length
R	thermal resistance
T	temperature (K)
U_L	overall heat loss coefficient
W	width of plate (m)
α	absorbance
ε	emissivity
η	efficiency
σ	Stefan-Boltzmann constant
τ	transmissivity
Kn	Knudsen number
k	thermal conductivity

improved building insulation in winter, and reduced solar gain in summer resulting in reduced air-conditioning loads in hot climates.

Beikircher et al. (2015) describes another approach for high efficiency flat plate collectors at medium temperatures (70–120 °C). Topside air conduction is reduced by a wide air gap with intermediate glass or plastic films to inhibit convection. Benz et al. (1996) examines the advantages of krypton to reduce heat loss in a low pressure (1–10 kPa) enclosure. Buttinger et al. (2010) developed a concentrating reflector encased in a deep evacuated flat enclosure with a pressure below 1 kPa. A combination of polysulphide and polybutyl rubber sealing was used and it was estimated that the internal pressure would rise from 60 Pa to 6 kPa after 20 years; outdoor testing demonstrated an efficiency of 50% for a krypton-filled collector when operating at 150 °C. Kim et al. (2013) tested a concentrating collector system based on evacuated tubes showing that the system can achieve more than 40% efficiency above 200 °C. Colangelo et al. (2016) reviewed a wide variety of alternative methods for increasing efficiency concluding that flat plate thermal collectors are the most widely used due to low cost and easy maintenance. There are some products commercially available (Benvenuti and Ruzinov, 2010; Abbate, 2012), however, many details of these commercial products are undocumented. The present work is to provide a detailed theoretical and practical guide for the fabrication of evacuated flat plate enclosures suitable for solar thermal applications.

The tests reported in this paper (part 1) were designed to demonstrate the ability of a prototype pillar-supported vacuum enclosure to maintain a high vacuum pressure and provide a high level of thermal insulation. The enclosure provides a 15 mm deep vacuum space suitable for accommodating a thin solar absorber; the absorber design is the subject of a parallel investigation at the University of Warwick (Moss et al., 2018a, 2018b, 2018c, 2017). The high level of thermal insulation and overall thickness of 14.2 mm would make such an enclosure (with or without an internal solar absorber) suitable for architectural use in a building façade.

2. Vacuum enclosure

The vacuum enclosure developed in this study consists of two glass panes hermetically sealed around their periphery to a stainless steel spacer, with the spacing maintained by support pillars to resist the influence of atmospheric pressure. This structure is similar in principle to vacuum glazing (Eames, 2008) though vacuum glazing typically uses a vacuum gap in the region of 0.25 mm and support pillars less than 1 mm diameter at a 20 mm separation. For solar collector applications the glass-glass separation is approximately 15 mm to accommodate a liquid-cooled absorber plate. The maximum pillar separation depends on glass thickness, glass properties (annealed or tempered) and pillar diameter, and is typically 60 mm (Henshall et al., 2016). To minimise heat loss through radiation both glass panes in the vacuum enclosure have low emittance coatings on the internal glass surfaces. A complete vacuum solar collector would also utilise a spectrally-selective (low emissivity at long wavelengths) coating on the absorber.

Creating a hermetic seal around the periphery of the glass panes and maintaining the separation of the glass panes under the influence of atmospheric pressure are significant challenges in the fabrication of vacuum flat plate collectors. The edge seal must be strong enough to withstand the stresses from atmospheric pressure and thermal expansion/contraction over its lifetime (Henshall et al., 2014).

The enclosure must be sufficiently vacuum-tight to maintain the desired vacuum pressure for the life of the collector and avoid any degradation in performance. The fabrication methodology and material choice are critical. Components in contact with the internal vacuum must be vacuum compatible otherwise outgassing would raise the internal pressure (Arya, 2014). The conceptual layout of a flat vacuum enclosure is shown schematically in Fig. 1(a). The pressure difference

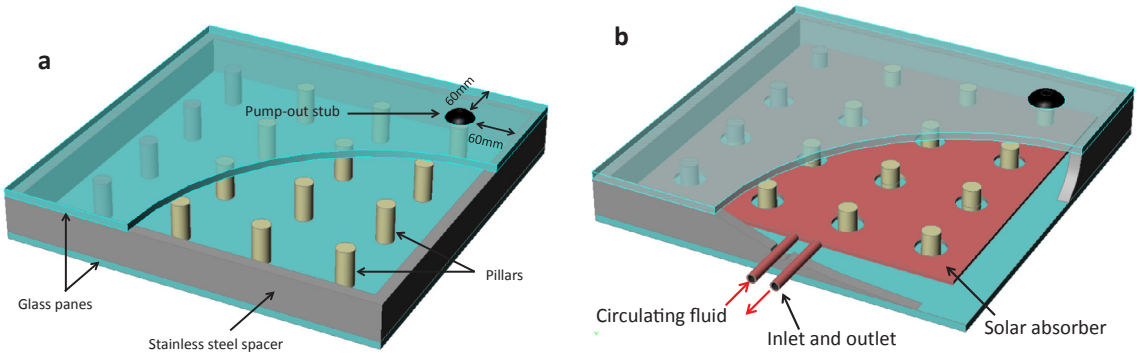

Fig. 1. Schematic diagrams of a flat vacuum enclosure (a) and a flat plate vacuum collector (b).

between external air and the internal evacuated space exerts large forces on the glass panes. An array of stainless steel support pillars is required to prevent glass breakage, excessive distortion or the risk of seal leakage. Two types of prototype vacuum enclosures have been fabricated at Ulster University. Fig. 1(a) illustrates a vacuum enclosure while Fig. 1(b) illustrates the enclosure incorporating an absorber plate.

3. Fabrication process

Selection of an appropriate sealing material is crucial to the fabrication of durable vacuum enclosures. The sealing material must form a mechanically strong bond between glass and the edge spacer, which is typically stainless steel and should have a low outgassing rate. In this work Cerasolzer 217 (a tin-based alloy) is used as the sealing material to create a hermetic seal between glass panes and edge spacer. Cerasolzer 217 is vacuum compatible, lead-free and can create a strong bond with both glass and stainless steel (Bellex, 2016). The sealing process is undertaken at 217 °C with manual tinning of the glass and spacer surfaces using an ultrasonic soldering iron (Hyde et al., 2000) followed by fusion of the tinned faces in an oven. After formation of the edge seal the enclosure is evacuated.

4 mm thick Pilkington K-glass (0.4 × 0.4 m) with an emittance of 0.16 was used for the enclosures; the chosen thickness was based on previous experience with vacuum enclosures (Arya et al., 2015). Whilst commonly used in insulating glazing, the high absorbance of K-glass renders it unsuitable for use in high-efficiency flat plate solar collectors. The choice of K-glass for the vacuum enclosures in this work was purely for convenience, however, this does not detract from the experimental purpose of demonstrating vacuum sealing and insulation improvements. The glass panes were cut to size (400 mm by 400 mm) and a hole (4 mm in diameter) was drilled in one pane close to the corner as a pumping port prior to tempering.

Fabrication of a vacuum enclosure requires all components to be thoroughly cleaned as any contamination on the internal surfaces will outgas resulting in an increase in pressure degrading the vacuum's insulation properties. The cleanliness of the glass panes in particular is crucial as the large surface area has the potential for increasing outgassing rates. In addition, any remaining contamination on the glass surface will prevent the formation of a strong and vacuum-tight bond between the sealing material and the glass. The glass panes were hand cleaned using a sequence of acetone and isopropanol, then washed in deionised water in an ultrasonic bath followed by baking in a conventional oven at 200 °C for 5 h. The support pillars and the stainless steel edge spacer were polished using a fine dry emery paper (800 grit) and were swabbed with diluted hydrochloric acid (33%) to remove any oxide layers (Lewis, 1995) and rinsed with deionised water. To minimise contamination of the glass, spacer and pillars the fabrication process was undertaken in a clean environment immediately following the cleaning processes.

In the enclosures 304L stainless steel was used for the support pillars and the edge spacer due to vacuum compatibility and frequent use in ultrahigh vacuum systems (Sgobba, 2006). However, 400-series stainless steel has a thermal expansion coefficient closer to soda-lime glass and was subsequently adopted when making complete solar collector assemblies. The spacer was cut as one piece from a 15 mm thick stainless steel sheet using a water jet machine.

After cleaning, a thin 10 mm wide layer of Cerasolzer 217 was deposited around the periphery on one face of each glass pane using an ultrasonic soldering iron to promote good adhesion. Similarly, a thin layer of Cerasolzer 217 was deposited on both faces of the spacer. The ultrasonic waves clean and remove the oxide layers from the surface of the substrates and force the molten material into any surface imperfections and micro-pores of the substrates to improve adhesion and bond strength (Bellex, 2016).

The support pillars, 15.2 mm high and 6 mm in diameter, were positioned upright on the lower glass pane at a 50 mm pitch as shown in Fig. 2a. The spacer was positioned on the lower glass pane so that the Cerasolzer layers were aligned. The upper glass pane was located over the spacer and the assembly was introduced into a bake-out oven. The oven temperature was increased at a rate of 5 °C per minute to 250 °C which formed the seal by Cerasolzer reflow. Following this the oven was allowed to cool to room temperature. A close visual inspection revealed gaps smaller than 0.05 mm at several locations in the seal. To minimise the impact of these gaps an additional layer of Cerasolzer was applied over the sealing area using an ultrasonic iron. The sealing process was undertaken below 250 °C to avoid de-tempering of the glass panes.

Following edge sealing of the enclosure a pump-out device was positioned over the pump out hole as shown in Fig. 2b and was connected to a turbo molecular pump. During the pump-out process the vacuum enclosure was heated at 150 °C for 7 h in a bake-out oven to outgas the internal surfaces (Arya et al., 2014). This heating regime can result in a durable vacuum, however, to have a vacuum which lasts over the service life of the enclosure it is necessary to integrate getters in vacuum enclosures to remove any residual gas in the vacuum space (Benvenuti, 2013). Achieving an ultimate vacuum pressure of 0.0021 Pa the pump-out hole was sealed with an indium-coated stainless steel disc; this process is described elsewhere (Zhao et al., 2007). Indium metal has been used in vacuum glazing as a sealing material (Hyde et al., 2000). Since indium is susceptible to oxidation in air, after completing the fabrication process all exposed edges were protected by a layer of epoxy resin (JB Weld, 2014). The pump-out sealing arrangement enabled the enclosure to be unsealed and resealed as required. During hot box testing this was used to create a range of internal pressures in the enclosure i.e. high vacuum (0.0021 Pa), low vacuum (8.4 Pa) and no vacuum (atmospheric pressure).

The evacuation process induces large stresses across the vacuum enclosure resulting from atmospheric pressure. The magnitude of the stress is larger near the support pillars and the edge seal similar to vacuum glazing (Fischer-Cripps et al., 1995). A visual inspection of the edge seal showed no signs of failure under these stresses, hence it was concluded that Cerasolzer 217 provided an adequately strong bond. The vacuum enclosure is shown in Fig. 3.

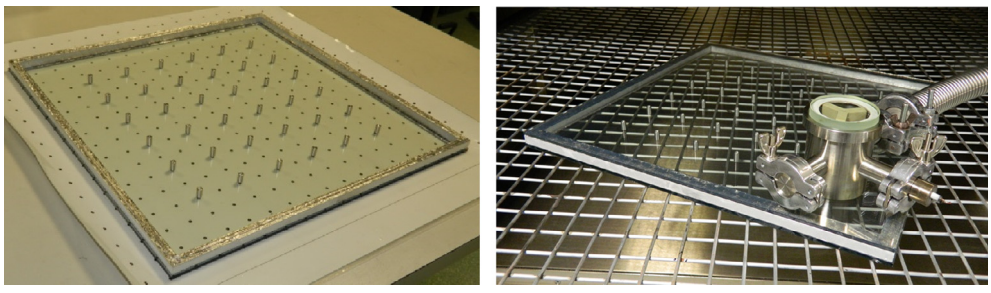

Fig. 2. Support pillars spaced on lower glass pane (a), enclosure pumped down via a pump-out system (b).

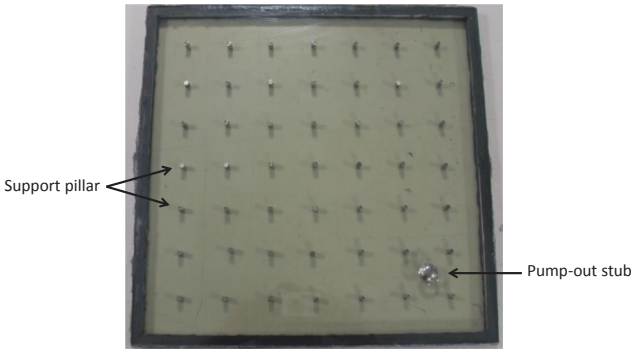

Fig. 3. The vacuum enclosure after fabrication.

4. Heat transfer in a vacuum enclosure

Heat transfer between the two glass panes in a flat evacuated enclosure occurs by radiation between the internal glass surfaces and conduction through the support pillars and the edge spacer. Any residual gas in the cavity will also contribute to heat transfer between the glass panes by conduction and, if above 10 KPa, by convection (Benz and Beikircher, 1999). The thermal conductivity of a perfect gas is not a function of pressure provided the pressure is sufficient for the molecular mean free path to be much less than the distance between the surfaces exchanging heat. The ratio of the molecular mean free path length to a representative physical length (d) is defined by the Knudsen number (Kn) which is a dimensionless number and is a function of the gas temperature and pressure:

$$Kn = \frac{0.008313}{\left(1 + \frac{116}{T}\right)pd} \quad (1)$$

At very low pressures the mean free path increases; if it becomes large compared to the gap (distance between the surfaces exchanging heat), the effective thermal conductivity will be much less than the standard value (Beikircher et al., 1996; Kennard, 1938). The conductivity multiplier f (Eq. (2)) such that $k_{lowpressure} = f \times k_{normal}$ is a function of the Knudsen number. The correction factor, f, is a function of the Knudsen number:

$$f = \frac{1}{1 + 3.75Kn} \quad (2)$$

If the gap is enlarged, the effective conductivity will increase unless there is a corresponding reduction in the pressure p to increase the mean free path; pressure × distance (pd) can determine whether or not the conductivity depends on the pressure. For example, solar collector operation with an ambient temperature of 20 °C and absorber temperature 80 °C would imply a mean residual gas temperature of 50 °C; at this condition $pd = 0.00255$ Pa·m is predicted to reduce the conductivity to 10% of its normal level. This is equivalent to 2.55 Pa for a 1 mm gap or 0.255 Pa for a 10 mm gap. Below this level ofpd the effective conductivity is approximately proportional to pd (Collins et al., 1995), and the heat loss will be proportional to $\frac{k}{d} \propto \frac{pd}{d} \propto p$ (see Fig. 4).

Solar thermal collectors are likely to use a larger gap between absorber and glass than the typical glass-glass gap in conventional vacuum glazing. They therefore require a lower pressure to achieve the full advantage of the vacuum in reducing heat losses from the absorber. When the pressure is low enough, the heat losses do not depend on the gap thickness.

5. Investigation of heat transfer in the vacuum enclosure

Conduction through the support pillars and edge spacer can contribute to heat flow through a flat vacuum enclosure; radiative heat transfer between the internal glass surfaces will also occur, regardless of the pillar and edge seal conductivity. In addition, any remaining gas will increase the overall heat transfer through the enclosure. The conduction processes may be investigated experimentally by creating a temperature difference between the two sides of a vacuum enclosure. Infra-red thermography techniques can reveal the “thermal bridges” where conduction occurs through the edge seal and pillars. The overall thermal transmittance of a flat vacuum enclosure can be accurately measured using a guarded hot box calorimeter. In the context of a solar thermal collector, heat transfer between front and back of the enclosure is less important than between absorber and enclosure surfaces. Both glass panes’ temperature will typically be close to ambient temperature whilst the absorber is hotter. Minimal contact between the absorber and the enclosure minimises conduction while low-emissivity coatings (and the absence of gas) reduces radiation and gaseous heat transfer as far as possible.

An experiment was designed to prove the efficacy of the vacuum in reducing heat transfer. The vacuum enclosure having just the two glass panes and a single stage of heat transfer allows a direct measurement of surface temperatures and facilitates interpretation. The results are also of interest since an evacuated solar thermal collector with glass on both sides could form an aesthetically enhanced building facade element and would have a thermal insulation role in addition to solar shading and heat generation.

5.1. Instrumentation

The thermal conductance of the fabricated vacuum enclosures was measured in a guarded hot box calorimeter available at Ulster University, shown in Fig. 5. The hot box calorimeter was designed in accordance with the relevant ISO and British Standard methods for determining thermal insulating properties (BS EN ISO 8990: 1996; BS 874: Part 3: Section 3.1: 1987).

The hot box calorimeter comprises warm and cold chambers separated by a well-insulated mask wall. As shown in Fig. 5, a metering box with known thermal properties is located inside the warm chamber. The vacuum enclosure is mounted in an opening through the mask wall. The temperature in the cold chamber is maintained below ambient by a chiller. Input power is supplied to the circulation fans and heaters inside the metering box to offset the heat loss to the cold chamber and create a temperature difference between the two sides of the test sample i.e. the vacuum enclosure while fans ensure uniform temperatures within each chamber. The power input is accurately measured. A matt black copper baffle is located in each chamber either side of the mask wall so that the radiant source temperatures for heat transfer to the enclosure are well known and unaffected by any thermal non-uniformity due to heaters, chillers and fans. The metering box and the surrounding warm chamber are maintained at the same temperature minimising heat exchange between them; consequently the heat in the

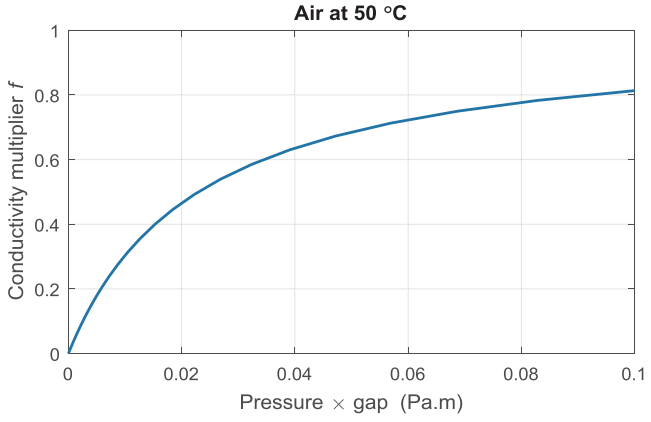

Fig. 4. Effect of pressure on effective conductivity.

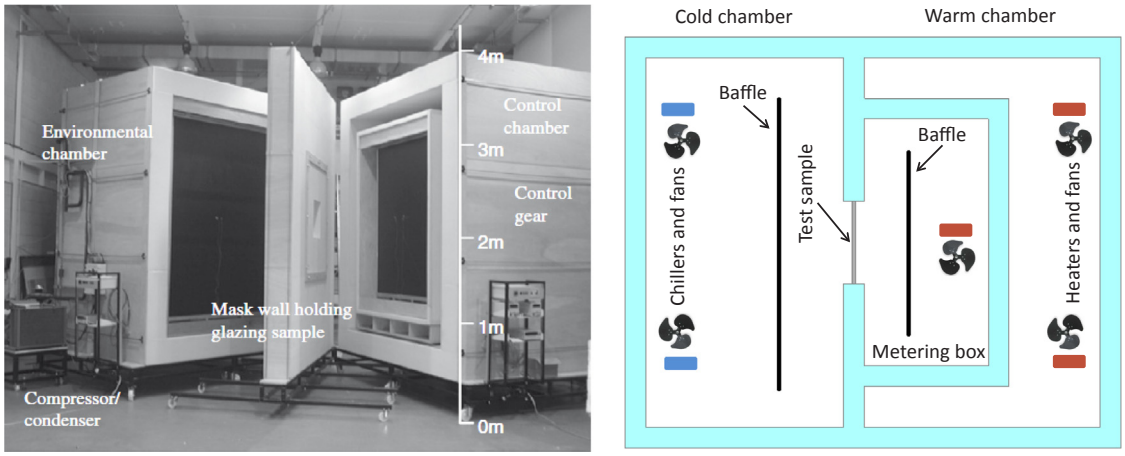

Fig. 5. Guarded hot box calorimeter at Ulster University.

metering box passes through the mask wall and the test sample into the cold chamber. By measuring the temperature within the metering box and the cold chamber, and the electrical power input to the heaters and fans, an accurate measurement of the heat flow through the test sample is possible. The hot box calorimeter is described in more detail by Fang et al. (2006).

The effect of vacuum pressure on the thermal performance of the vacuum enclosure was investigated at three pressures; 0.0021 Pa, 8.4 Pa and at atmospheric pressure. These vacuum pressures were maintained using a turbo molecular pump (Edwards T-Station 75 with pumping rate of 42 L/s) and rotary pump (Leybold). The vacuum pressure was measured using vacuum gauges (Leybold: PTR 90 PENNINGVAC for high vacuum and Leybold: TR-211 PIRANI for low vacuum) which were connected to the pump-out device via a Tee-connection.

The vacuum enclosure is positioned in the opening through the mask wall as schematically shown in Fig. 5. Eight thermocouples are attached to each side of the enclosure along the centre line (Fig. 6) to monitor surface temperature. Due to conductive heat flow through the support pillars there is an uneven surface temperature distribution in the region of the support pillars, therefore the thermocouples were attached to the glass surface remote from the pillars (Fig. 6).

The measured glass surface temperature, air temperature in the metering box and cold chamber, baffle temperatures and the heat flows through the test samples are presented in Table 1 for the three vacuum pressures investigated. The temperature difference between the glass panes of the vacuum enclosure with a high vacuum is larger than that in the other tests, indicating the higher the vacuum, the lower the heat loss would be.

5.2. Enclosure conductance and U-value measurements

The hot box instrumentation records mean air, baffle and glass surface temperatures on each side of the test panel together with the heat flux through the panel (Table 1). The thermal conductance of the test sample, C-value, is given by:

$$C = \frac{Q}{A(T_{s1} - T_{s2})} \tag{3}$$

Q is the heat flow through the 0.4 × 0.4 m enclosure with area A = 0.16 m^2 and T_s is the mean surface temperature on either side of the enclosure. The conductance in Table 1 is based purely on the thermocouple temperature readings. The true mean surface temperature will differ from the thermocouple mean due to local effects around the pillars; the effect of this on C and U-values is discussed later.

Two definitions of U-value (overall heat transfer coefficient, allowing for thermal resistance between the glass covers and surroundings on both sides of the sample) have been used and are defined: (1) the hot box U-value is determined at conditions within the hot box calorimeter, and (2) the declared U-value uses standard heat transfer coefficient values on each side of the sample. The hot box U-value (Fang et al., 2006) is given by:

$$U = \frac{Q}{A(T_{n1} - T_{n2})} \tag{4}$$

The U-value for the sample in the hot box colorimeter is dependent on the heat transfer coefficients either side of the sample due to radiation and convection in addition to the conductance of the sample. T_{n1} and T_{n2} are the environmental temperatures in the hot and cold chambers respectively, given by:

$$T_n = \frac{T_a \frac{Q}{A} + \varepsilon h_r (T_a - T_r) T_s}{\frac{Q}{A} + \varepsilon h_r (T_a - T_r)} \tag{5}$$

T_n is a weighted mean of the air (convection) and baffle (radiation) temperatures such that any variation of heat flux with sample surface temperature can be expressed accurately in terms of an environment temperature and a heat transfer coefficient, the latter effectively combining the heat transfer coefficients due to radiation and convection. For radiation calculations, only the matt black copper baffles are considered since they occupy 90% of the test samples view angle with a view factor of 0.895 (Arya, 2014). The mean radiant temperature T_r is taken to be the baffle temperature. The effective emissivity ε_{12} is determined using the emissivity of the test sample (vacuum enclosure) ε_2 and the baffle ε_1 (for the matt black baffle ε_1 is 0.97):

$$\frac{1}{\varepsilon_{12}} = \frac{1}{\varepsilon_1} + \frac{1}{\varepsilon_2} - 1 \tag{6}$$

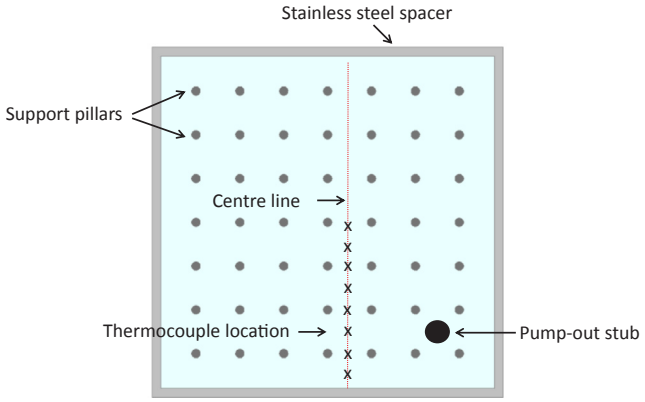

Fig. 6. Thermocouple positions ('x') on the test sample during testing in the hot box calorimeter.

Table 1
Air temperatures in the guarded hot box calorimeter and measured U-values for the flat vacuum enclosure.

Sample		Mean air temperature (°C)	Mean baffle temperature (°C)	T_n (°C)	Mean thermocouple temperature (°C)	ΔTg	$\dot{q}$ (W/m^2)	C-value (W/m^2 K)	U-value (W/m^2 K) (hot box)	U-value (W/m^2 K) (declared)
No vacuum	Cold	−0.7	−0.14	−0.57	1.8	9.15	43.8	4.78	2.35	2.64
	Warm	17.96	17.95	17.95	10.95					
Low vacuum (8.4 Pa)	Cold	−0.91	−0.51	−0.82	1.17	11.07	36.3	3.27	1.91	2.10
	Warm	18.05	18.01	18.02	12.24					
High vacuum (0.0021 Pa)	Cold	−0.51	−0.35	−0.47	0.91	13.69	25.6	1.87	1.35	1.42
	Warm	18.47	18.43	18.44	14.6					

The radiative heat transfer coefficient, h_r, can be calculated using:

$$h_r = 4\sigma T_l^3$$

σ is the Stefan-Boltzmann constant (5.67×10^{-8} W/m^2 K^4), and T_l is the mean radiant temperature given by:

$$T_l^3 = \frac{(T_r^2 + T_s^2)(T_r + T_s)}{4} \quad or \quad T_l \approx \frac{T_r + T_s}{2} \tag{7}$$

T_r, T_l and T_s are expressed in Kelvin. Whilst the radiative heat transfer coefficient h_r may be calculated from first principles, the convective equivalent cannot be accurately described by standard correlations as it will depend on the pattern of air flow within the chambers and the thermal boundary layers over the enclosure surfaces. The advantage of Eqs. (1) and (2) is that they avoid any need to determine the convective heat transfer coefficient at the sample surface (British Standards Institution, 1987; ISO, 1994). Once T_{n1} and T_{n2} have been determined the effective heat transfer coefficients on each side (j = 1, 2) may be calculated to show the combined convective and radiative effect:

$$h_j = \frac{Q}{A(T_{nj} - T_{sj})} \tag{8}$$

The hot box test data shows h_{cold} = 18.4 W/m^2 K and h_{warm} = 6.4 W/m^2 K over the three vacuum conditions investigated, based on an assumption that the thermocouples give an accurate measure of the surface mean temperature; the 90% confidence limits based on a standard error of the three tests are ± 1.4% and ± 6.3%, respectively. An alternative form of U-value is defined in BS EN 675 to allow for comparisons between U-values measured in different facilities or via heat flux meter measurements on buildings. The declared U-value is:

$$U = \frac{1}{\frac{1}{C} + \frac{1}{h_e} + \frac{1}{h_i}} \tag{9}$$

BS EN 675 specifies standard values h_e = 25 W/m^2 K and h_i = 7.7 W/m^2 K for the external and internal heat transfer coefficients, respectively. The hot box test data is presented in Table 1 together with the C-values and U-value determined using both approaches. For reference, the relationship between enclosure conductance and U-value is shown in Fig. 7.

5.3. Conductance and U-value predictions

The measured U-value of the enclosure prior to evacuation was 2.35 W/m^2 K; this is comparable to the thermal performance of a conventional double glazing of equivalent size and configuration in terms of glass and seal characteristics. After evacuating the cavity, gaseous convective and conductive heat transfer was reduced, resulting in heat transfer coefficients down to 1.91 W/m^2 K and 1.35 W/m^2 K for 8.4 Pa and 0.0021 Pa, respectively.

5.3.1. Comparisons with vacuum glazing U-value and models

Conventional vacuum glazing typically uses support pillars that are much smaller in diameter than the glass thickness. A thermal analysis that models each glass pane as a semi-infinite solid (Collins and Simko, 1998) then estimates the pillar array contribution to the glazing's thermal conductance as:

$$C = \frac{2k_{glass}a}{P^2} \tag{10}$$

Thus the support pillars (0.4 mm diameter, 0.15 mm high and at 20 mm separation) in a typical vacuum glazing are therefore expected to contribute 1 W/m^2 K towards the overall thermal conductance. Radiative heat exchange and residual gas conduction between the glass panes will add to the pillar conductance. The heat flux due to radiative heat transfer between two infinite parallel plates is given by: $\dot{q}_{12} = \varepsilon_{12}\sigma(T_1^4 - T_2^4)$ with an effective emissivity of $\varepsilon_{12} = \left(\frac{1}{\varepsilon_1} + \frac{1}{\varepsilon_2} - 1\right)^{-1}$. The vacuum enclosure used two low emissivity glass panes (ε = 0.16) with the coatings facing inwards to give an effective emissivity of ε_{12} = 0.087 and radiative conductance of $C_{rad} = \varepsilon_{12}\sigma(T_1 + T_2)(T_1^2 + T_2^2)$ = 0.43 W/m^2 K at typical temperatures during testing. Combining the pillar conductance and radiative terms for vacuum glazing gives: $C_{pillararray} + C_{Rad}$ = 1.0 + 0.43 = 1.43 W/m^2 K, corresponding to a measured U-value (Fig. 7) of 1.1 W/m^2 K. For comparison, a U-value of 0.86 has been measured in this hot box calorimeter for vacuum glazing fabricated using similar low-e glass (Arya, 2014) suggesting that Eq. (10) over-predicts the pillar conductance effect. This may be due in part to a glass thickness of 4 mm thick, as opposed to semi-infinite, and the model does not include any thermal resistance at the contact points.

5.3.2. Prediction of conduction along pillars

The pillar diameter used in the fabricated vacuum enclosures (6 mm) is greater than the 4 mm glass thickness. The "semi-infinite glass" analysis based on pillar radius (Eq. (10)) becomes less appropriate when the glass is thin relative to the pillar radius; hence Eq. (10)

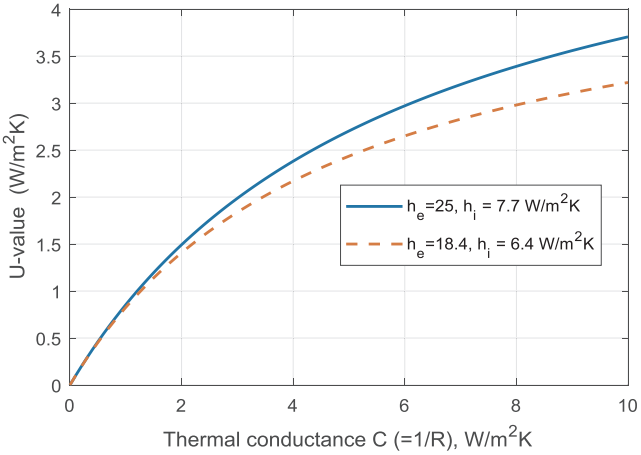

Fig. 7. Relationship between enclosure conductance and U-value for hotbox and BS EN 675 "declared" conditions.

would be likely to overestimate the conductance. The 3D conduction equations were solved using ABAQUS CAE ™, as shown in Fig. 8. The grid modelled a 90° segment of a pillar and its associated glass panes, using 3952 elements in each glass pane and 3024 in the pillar quadrant. External heat transfer coefficients and contact conductance at each glass-pillar interface (Table 2) were chosen to match the measured heat flux and thermocouple temperatures from Table 1. Some assumptions were necessary as the model attempts to define 4 parameters (three heat transfer coefficients and one contact resistance) based on only 3 measured variables.

A finite contact conductance is to be expected since deformation of the glass under vacuum will cause it to touch around the outer circumference or rim of the pillar; Hertzian contact stresses for a cylinder indenting a solid also indicate a pressure peak around the rim. This is expected to further concentrate the heat flux around the rim, above the levels due to 3D conduction in the glass, which will increase the thermal resistance for heat flux to the pillar. Arbitrarily adding a uniform contact conductance over the pillar end is a simple way of modelling the effect of this increased thermal resistance without knowing its radial distribution.

The first case analysed was the high vacuum condition (Table 2). For convenience in ABAQUS, the predicted 0.43 $W/m^2 K$ (Section 5.3.1) heat transfer coefficient across the vacuum space was modelled as two thermal resistances in series, using coefficients of 0.86 $W/m^2 K$ each side of an internal mid-plane with a temperature of 7.77 °C. Simulations using infinite conductance at the contact points between glass and pillar over-predicted the heat flux: a finite contact conductance at each pillar end of 2321 $W/m^2 K$ was necessary to reduce the heat flux to the experimental level.

Hot and cold side external heat transfer coefficients were chosen to match the mean thermocouple temperatures along the far (distant from the pillar) edge of the grid. Heat transfer to the cylindrical pillar surface was not modelled since the polished stainless steel surface has a low emissivity and the mean pillar temperature is very close to the mid-plane temperature. A trial simulation showed there to be no significant effect on the external temperatures and overall conductivity. The simulation results were in agreement with the total heat flux over the 0.4 × 0.4 m enclosure area. Thermal bridging through the edge seals might be expected to increase the measured heat flux per unit area over what would be achieved for an infinitely large enclosure (Fang et al., 2007). The fact that a realistic simulation of the high-vacuum test can be achieved without raising the internal heat transfer coefficient above the expected radiative level suggests that edge effects are not significantly affecting the experimental results.

The effect of the contact conductance is visible as a temperature difference between the inner surface of the glass and the pillar end in Fig. 8(b). The temperature difference through the glass falls from approximately 2.4 °C above the pillar end to 0.06 °C at the edge of the grid. Comparison of the xz and diagonal planes shows that the temperature distribution is very close to axi-symmetric. The temperature contours, Fig. 8(a), shows that symmetry is only lacking in the far diagonal corner, where there is an approximately circular high temperature contour centred on the grid corner. The boundary conditions required to match the experimental temperatures are given in Table 2. Hot and cold air temperatures and heat flux match the hot box high vacuum condition (Table 1) in the U-value test.

Heat flux was matched within 0.13% and temperatures within 0.04 °C. Hot-box U-values are unchanged from Table 1 as they are not dependent on surface temperature measurements. The conductance of the pillar array is C = 1.26 $W/m^2 K$. This is higher than the 1.0 $W/m^2 K$ for the pillars in typical vacuum glazing. Both vacuum glazing and evacuated enclosures can achieve internal heat transfer coefficients of 0.43 $W/m^2 K$ under high vacuum conditions. The higher pillar array conductivity in a vacuum enclosure leads to higher C- and U-values than in vacuum glazing. These increased C- and U-values could be overcome by using a lower conductivity material for the pillars such as glass (k = 1 W/m K). Repeating the high vacuum simulation with the pillar conductivity lowered to 1 W/m K to represent glass pillars (fourth row in Table 2) instead of stainless steel pillars produced a declared U-value of 0.82 $W/m^2 K$.

Under high vacuum conditions the heat transfer route is conduction through the pillars. Under low vacuum and no vacuum conditions the internal heat transfer coefficient (h_{gap} in Table 2) rises and the pillars transfer a smaller fraction of the total heat flux, as shown by the $\frac{\dot{q}_{pillar}}{\dot{q}_{total}}$ values. When modelling the low vacuum scenario the contact conductance was assumed unchanged as there would be a negligible difference in the contact force between glass and pillars. Under the "no vacuum" conditions there is a significant increase in heat flux due to gas conduction. Within sensible heat transfer coefficient limits, this could only be achieved by assuming an almost negligible contact resistance at the end of each pillar; an arbitrary conductance of 100 $kW/m^2 K$ was chosen. Matching the thermocouple measurements to the FE solution, as opposed to assuming that the thermocouples accurately represent the mean surface temperature, leads to the modest difference in C-values and declared U-values between Tables 1 and 2.

5.3.3. Internal heat transfer coefficient discussion

The heat transfer coefficient between the internal glass surfaces is

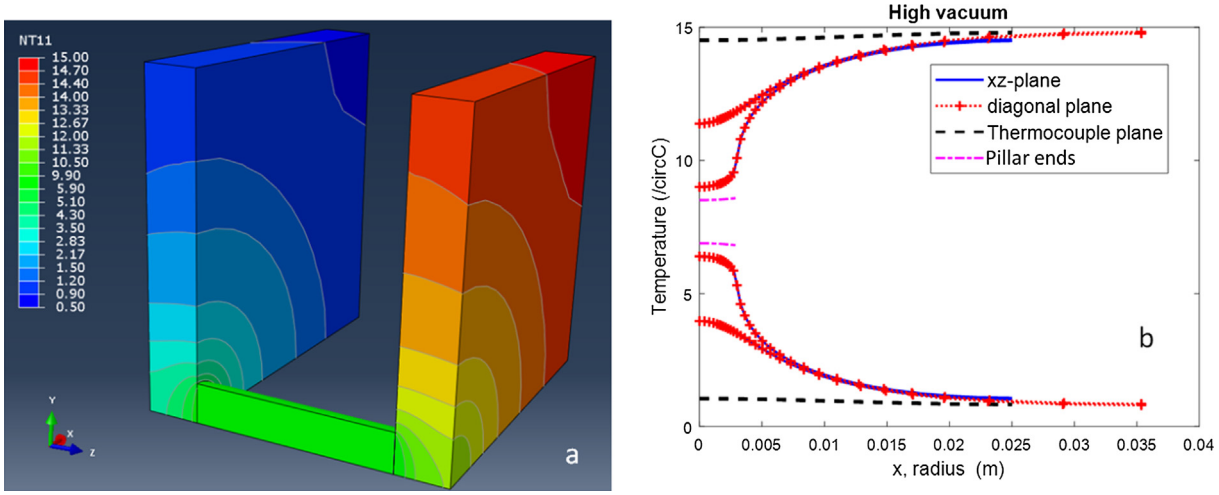

Fig. 8. Temperature field predictions for a repeating section based on one quadrant of a pillar. (a) Contours (°C) (n.b. unequal intervals), (b) Glass and pillar surface temperatures on planes between grid corners. The diagonal plane runs between opposite corners and is plotted against radius.

Table 2
Simulation conditions to match Table 1 thermocouple temperatures and heat fluxes. Units are W/m² K unless stated (heat flux fraction is dimensionless; pillar heat flux is per unit area of glass). ΔT describes the range of temperature variation on the outer face of the cold pane (see Table 3).

	h_{cold}	h_{gap}	h_{hot}	Contact conductance	Pillar heat flux (W/m²)	$\frac{q_{pillar}}{q_{total}}$	Cold ΔT (°C)	C-value (W/m² K)	U-value (W/m² K) (declared)
No vacuum	16.59	3.352	6.1	100,000	16.1	0.368	2.29	5.22	2.77
Low vacuum (8.4 Pa)	15.8	1.935	6.08	2321	16.6	0.457	2.48	3.51	2.20
High vacuum (0.0021 Pa)	14.5	0.43	6.1	2321	20.2	0.789	3.16	2.00	1.49
High vacuum (0.0021 Pa) with glass pillars	14.5	0.43	6.1	2321	8.12	0.554	1.27	0.95	0.82

expected to be the sum of a radiative component, 0.43 W/m² K, and a conductive and convective component. For pure conduction, the ratio of convective to conductive heat transfer (the Nusselt number) is 1. The Nusselt number (Nu) is defined as $Nu = \frac{hd}{k}$ where h is the heat transfer coefficient, d is the characteristic length and k is the thermal conductivity. At atmospheric pressure this gives h = 1.63 W/m² K. In the presence of natural convection driven by the temperature difference between the hot and cold surfaces the Nusselt number will exceed 1; the heat transfer coefficient is then $h = Nu\frac{k}{d}$.

The convective Nusselt numbers in vertical-faced tall enclosures have been studied with regard to double glazing (Ganguli et al., 2009). At low vacuum condition the Raleigh number is too low for convection to occur. Eq. (2) predicts the air conductivity to be 15% lower at 8.4 Pa than at 100 kPa, so the glass gap heat transfer coefficient is expected to be$0.85 \times 1.63 + 0.43 = 1.82$ W/m² K. It is considered the value of 1.935 W/m² K used in the simulation (Table 2) is within the limits of acceptability.

At typical hot box test conditions with a temperature difference between the hot and cold surfaces of ~10 °C, the Raleigh number at 10^5 Pa pressure is $Ra_L = 3500$ (based on a gap of 15.2 mm). 2D flow simulations (Ganguli et al., 2007) suggest that this Raleigh number is at the lower limit for a multi-cellular convection regime; there is no evidence of this in the IR images (Section 5.4); it may be impeded by the finite width and the presence of the pillars. For a tall and vertical sided enclosure the convection at this Raleigh number causes only a modest increase in Nusselt number above the $Nu = 1$ corresponding to pure conduction. The correlation by Ganguli et al. (2009), $Nu_L = 0.151 Ra_L^{0.3}(AR)^{-0.164}$, predicts $\bar{Nu}_L = 1.035$ at this condition. The glass gap heat transfer coefficient at ambient pressure is therefore expected to be no more than $1.035\frac{k}{d} + 0.43 = 2.13$ W/m² K. The value required by the simulation, 3.352 W/m² K, is unexpectedly high; the reasons for this high value are not fully understood but may be related to the use of local (thermocouple) temperatures in the simulation instead of a mean surface value. At atmospheric pressure the Grashof number is $Gr_H \approx 1.38 \times 10^8$. In the presence of internal convection the assumption of equal heat transfer coefficients between adjacent surfaces may not be valid. The change in thickness of the thermal boundary layer as the circulating flow moves up the hot face and down the cold face should lead to higher hot and lower cold heat transfer coefficients in the bottom half of the enclosure.

5.3.4. Analytical modelling of glass temperatures using an axi-symmetric model

The 3D simulation shows that the temperature distribution on the inner and outer faces of each glass pane is approximately axi-symmetric. It should therefore be possible to predict the temperatures as a thin sheet radial conduction problem. For simplicity, the 50 × 50 mm square of glass associated with each pillar will be modelled as a circular disk of the same area (diameter: $\sqrt{4/\pi} \times 50 \approx 56.4$ mm) with heat removal at the pillar radius of 3 mm. The temperature field is described by Bessel's equation:

$$r^2\frac{d^2T}{dr^2} + r\frac{dT}{dr} - \frac{h}{kt}r^2T = -\frac{h}{kt}r^2\left[\frac{G'}{h} + T_{ad}\right] \tag{11}$$

h is the heat transfer coefficient to surroundings at a temperature of T_{ad}, t and k are thickness and thermal conductivity of glass and G' is the rate of heat dissipation in the glass due to absorption of radiation. r is the distance from the centre of the support pillar. T_{ad} is the glass equilibrium (adiabatic) temperature in the absence of any pillar heat flux. For the simple case of a single glass pane with known temperature (1, 2) on each side, T_{ad} and the combined heat transfer coefficient h are defined by:

$$T_{ad} = \frac{h_1T_1 + h_2T_2}{h_1 + h_2} \tag{12}$$

where $h = h_1 + h_2$. The heat transfer coefficients h_1, h_2 represent the cold side and gap, or gap and the hot side coefficients as used in Table 2. As in the finite element (FE) prediction, the internal heat transfer coefficient is doubled ($h_2 = 2h_{gap}$) and refers to a central reference plane temperature T_2; this allows the equations for each pane to

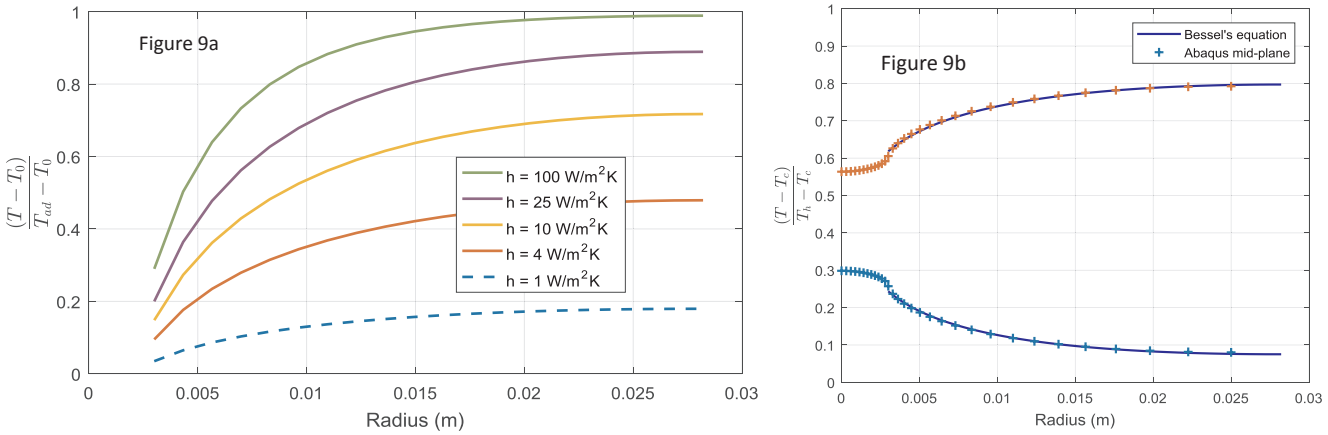

Fig. 9. Radial temperature distributions due to heat flux through a support pillar, modelling the glass as a thin circular disk. (a) Single-sided case, (b) Double-sided asymmetric case comparing the 3D and Bessel's equation solutions at the high vacuum conditions in Table 2.

be solved independently, albeit with some iteration to determine the reference plane temperature. The substitution of $z = \sqrt{h/kt}\,r$ simplifies Eq. (10):

$$z^2\frac{d^2T}{dz^2} + z\frac{dT}{dz} - z^2T = z^2\left[\frac{G'}{h} + T_{ad}\right] \tag{13}$$

The solution in terms of modified Bessel functions is $T = AI_0(z) + BK_0(z) + \frac{G'}{h} + T_{ad}$ where A and B are constants to be determined from the boundary conditions. When modelling the hot box tests there is no illumination and hence $G' = 0$. The first boundary condition is to achieve zero radial heat flux at the outer radius, r_2. This is necessary for symmetry at the interface between pillar zones:

$$AI_1(z_2) - BK_1(z_2) = 0 \tag{14}$$

The second boundary condition sets a given temperature at the inner radius r_1 i.e.

$$T_{z1} = AI_0(z_1) + BK_0(z_1) + \frac{G'}{h} + T_{ad} \tag{15}$$

This pair of simultaneous equations is solved to determine the constants A and B. The radial temperature distribution $T(z)$, area-weighted mean temperature $\bar{T}$ and heat flux Q at the inner radius can then be determined; $Q_j = 2\pi z_1 kd(A_j I_1(z_1) - B_j K_1(z_1))$. Typical results for the temperature distribution in a single glass pane in contact with a half-length pillar are shown in Fig. 9(a). A thermal resistance calculation is then used to combine the hot and cold-side glass solutions and the pillar thermal resistance, Fig. 9(b).

A contact resistance of 0.0015 m^2 K/W was used in the Bessel's equation solution to achieve a good match with the 3D solution. This is equivalent to a 1.5 mm thickness of glass over each pillar end and is 3.5× the thermal resistance included in the high vacuum ABAQUS simulation. This additional thermal resistance is necessary because the thin-sheet Bessel's equation does not model temperature gradients through the thickness of the glass. The good agreement between the 3D finite element simulation and the much simpler analytical model suggests that the latter could find use as a design tool to rapidly assess the effect of changes in parameters such as glass thickness, pillar length, diameter, pitch and conductivity.

5.4. Infra-red thermography of vacuum enclosures

The temperature distributions in Figs. 8 and 9 results in a regular repeating pattern of higher temperature regions on an otherwise uniform temperature surface which can be detected using infra-red thermography. The hot box calorimeter previously described was used for IR thermography analysis of the vacuum enclosures. The cold chamber was removed and the vacuum enclosure was located in the mask wall and secured against the warm chamber as illustrated schematically in Fig. 10. The air temperature inside the warm chamber was maintained at 42 °C while the ambient temperature surrounding the chamber was 22 °C. The high chamber temperature (42 °C) was chosen to ensure the outer glass pane was above ambient temperature, thereby minimising reflected IR emissions from the laboratory environment. The infrared camera used in this experiment was a FLIR B640. The IR images were taken under steady-state conditions after the temperature difference between the two sides of the enclosure had stabilised.

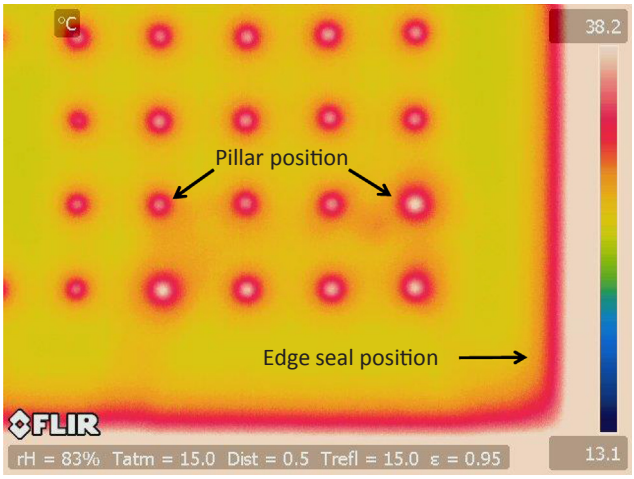

Fig. 11. IR image of one corner of the vacuum enclosure seen from the cold side (high vacuum test). The temperature scale assumes a nominal $\varepsilon = 0.95$.

Fig. 11 shows a typical IR-image of one corner of the vacuum enclosure. Thermal bridging through the pillars and the edge seal is evident from the increased surface temperature in these regions. The surface illustrated is the outer side of the cold pane i.e. equivalent to the bottom curve in Fig. 8(b). As glass is opaque to long wavelength infrared this represents a view of the visible surface as opposed to a view through the glass. The increased conduction through the edge seal and pillars is expected since the conductance of a stainless steel pillar (k/L = 16/0.015 ≈ 1000 W/m^2 K for a 15 mm length) is much higher than the glass-glass radiative heat transfer coefficient, predicted before as 0.43 W/m^2 K under high vacuum conditions.

Infrared images of the cold-surface temperatures over the central region at 0.0021 Pa and 8.4 Pa are illustrated in Fig. 12 and at atmospheric pressure illustrated in Fig. 13. Comparison of the high and low

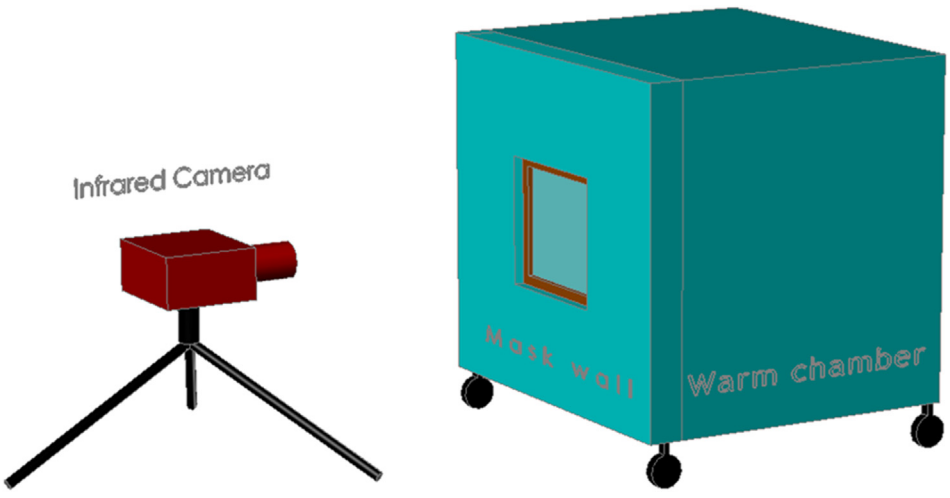

Fig. 10. Configuration for infra-red thermography.

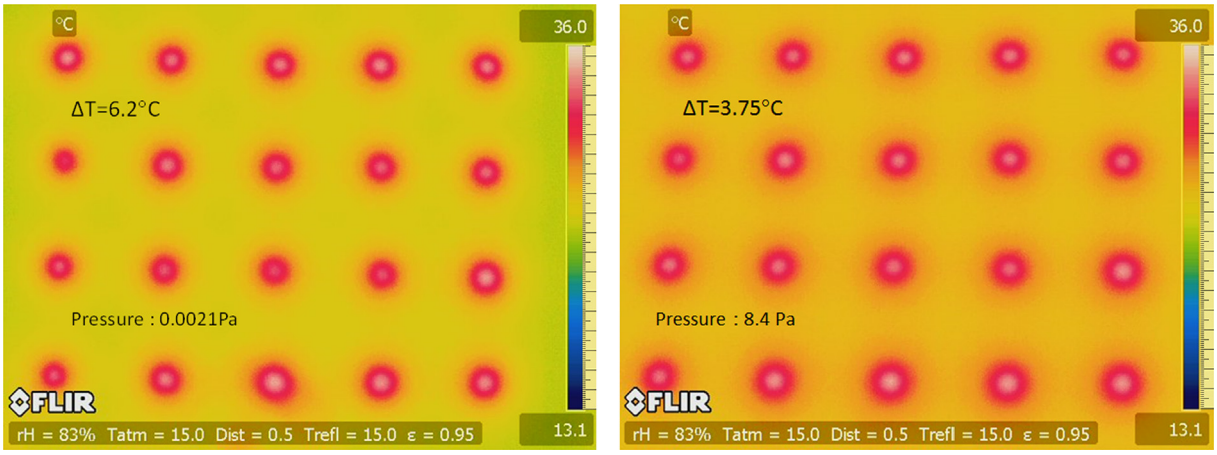

Fig. 12. Infrared images of the central region of the vacuum enclosure at different internal pressures: 0.0021 Pa (left) and 8.4 Pa (right), as seen from the cold side.

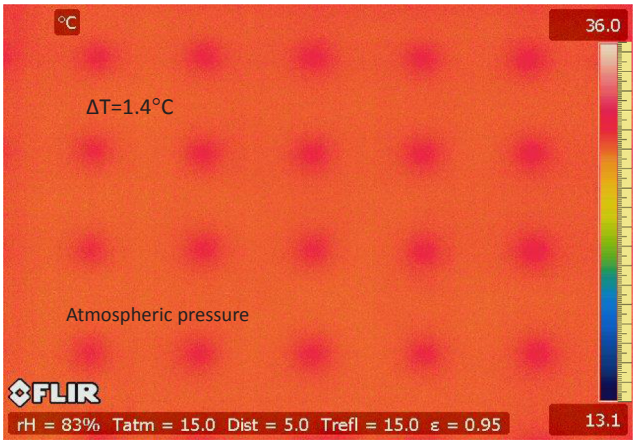

Fig. 13. Infrared image of the enclosure at atmospheric pressure.

vacuum conditions shows a drop in the cold-side temperature as the vacuum pressure is reduced. This is in agreement with the hot-box measurements showing a decrease in U-value with a reduction in internal pressure. A number of spot temperatures have been extracted from the images using the IR camera software and are summarised in Table 3.

For comparison, the expected variation on the cold face between local maxima and minima is included in Table 2 as "Cold ΔT" and is in the range of 2.3–3.2 °C. These simulations model the vacuum enclosure with the cold chamber in place. The temperatures on each side are higher during the IR tests, however the difference between hot and cold air temperatures is similar (18–19 °C during hot-box testing and 20 °C during the IR tests). During the IR thermography the cold chamber was removed resulting in free convection over the cold face compared to forced convection from the circulating fans during the hot box thermal transmittance testing. A laminar correlation for a mean Nusselt number over a vertical plane, $Nu_L = 0.56Ra_L^{0.25}$, suggests that the cold-side heat transfer coefficient due to natural convection is approximately 2.9 W/m^2 K. An equivalent ABAQUS simulation at the high vacuum condition gives a thermocouple-plane temperature of 28.23 °C and ΔT = 2.75 °C between hot and cold regions. The observed variation (6.2 °C) and typical temperature (23.4 °C) are significantly different to the high vacuum predictions. This may result from the adhesive used to locate the pillars on one of the glass panes. The small glue contact point may effectively reduce the pillar end diameter and lead to a larger temperature variation. Despite the fact that infrared thermography techniques provide valuable information, the data obtained is indicative only as measurements can easily be affected by environmental conditions such as reflections from surrounding surfaces.

Stainless steel has a significantly higher conductivity than air (16.2 versus ~ 0.025 W/m K), hence even if the enclosure contained air, it would be expected that the pillar contact points would result in higher temperatures compared to surrounding regions. Fig. 13 shows an infrared image of the vacuum enclosure taken at atmospheric pressure which clearly illustrates a small temperature variation (1.4 °C) across the enclosure with higher temperatures close to and above the pillars.

The general trend of the maximum to minimum temperature variation reducing in amplitude as the internal pressure increases may be correlated with the simulations in Table 2. In the high vacuum enclosure, radiative heat transfer between the low-emissivity ($\varepsilon = 0.16$) surfaces predicts a radiative thermal conductance of 0.43 W/m^2 K. However, if the gas pressure in the cavity is higher than the required level (1 Pa), conductive and convective heat transfer through the gas will be greater than the purely radiative heat transfer. For conduction over a distance of L in air (15 mm glass-glass gap and k = 0.025 W/m K), the thermal conductance, $C = k/L$, will be 1.66 W/m^2 K i.e. more than the pillar array thermal conductance (C = 1.26 W/m^2 K). Any decrease in overall thermal resistance will diminish the mean temperature difference between the glass panes as well as the local glass temperature perturbations around the end of each pillar. If the gaseous conduction was very high (which could occur with the small 15 mm gap in a vacuum enclosure if the vacuum seal failed) then the temperature variations would diminish until barely visible as demonstrated in Fig. 13. Fig. 12 exhibits variations in the temperatures directly over the support pillars. During the thermal glass tempering process the hot glass passes over rollers which leave a characteristic wave deformation after cooling, thus the glass is no longer flat. The rigidity of the glass is such that even a small variation in flatness or a small variation in pillar size (± 0.02 mm) may result in a large difference in compressive load between adjacent pillars causing variations in the thermal contact resistance. The safety margin is clearly high enough for the glass to resist breakage even when the load is not evenly distributed over all the pillars. This could be a useful experimental technique, if properly calibrated, for estimating the pillar to pillar load variation.

Creating a temperature difference between the two sides of the

Table 3
Temperatures extracted from infra-red images. The "thermocouple line" is shown in Fig. 2. ΔT is the temperature difference between the hot spot above a typical pillar and the cooler region away from the pillars.

	No vacuum	Low vacuum	High vacuum
"Thermocouple line" mean (°C)	30.2	25.6	23.4
Temperature variation ΔT (°C)	1.4	3.75	6.2

vacuum enclosure during calorimeter testing and infra-red thermography imposes differential thermal expansion stresses in the enclosure (Henshall et al., 2014). There are also in-built stresses due to differences in expansion coefficient as the enclosure cools from its fabrication temperature during edge sealing. In this study the solder proved mechanically robust to withstand these stresses. Further work is required to explore the safe stress limits and the potential to use thinner glass, smaller pillars or a wider separation between pillars.

6. Conclusions

A vacuum enclosure, suitable for use in solar collectors, was fabricated from 4 mm tempered Pilkington K-glass, a stainless steel edge spacer and a stainless steel pillar array. The enclosure was designed to accommodate a solar absorber plate which will be added in future analysis. To seal the enclosure, the joint surfaces were tinned with Cerasolzer 217 solder using an ultrasonic soldering iron. The solder layers were then fused in a bake-out oven. An epoxy resin overlay provides protection against moisture ingress and corrosion of the solder. The edge seal was sufficiently vacuum tight to enable a vacuum pressure of 0.0021 Pa to be achieved and strong enough to withstand atmospheric pressure and thermal expansion/contraction stresses resulting from temperature gradients across the enclosure or due to mismatched coefficients of thermal expansion between the glass and the stainless steel spacer.

Experimental characterization demonstrated the excellent thermal performance of the enclosure when evacuated; an overall thermal transmittance U-value of 1.35 $W/m^2 K$ was achieved. High efficiency solar collectors based on this enclosure design could therefore be incorporated into a building façade and would provide excellent thermal insulation for the building in addition to fulfilling their solar energy role.

Finite element and analytical models achieved good correlation with experimentally measured temperatures and heat fluxes using credible contact conductances and heat transfer coefficients. The finite element model indicates that declared U-values as low as 0.82 $W/m^2 K$ should be possible if the pillars could be made of a low conductivity material such as glass.

In vacuum glazing analysis, an increase in glazing size reduces the influence of the edge seal conduction on the overall thermal performance resulting in a lower heat transfer coefficient (Fang et al., 2007). However, in the case of the vacuum enclosure the heat transfer coefficient prediction with no edge effects is close to the experimental level suggesting that only a small improvement would be achievable relative to the 0.4 × 0.4 m enclosure test result. The reason is that the portion of heat flow through the edge seal in vacuum glazing is larger than that of the vacuum enclosure due to the low conductance of the rest of the vacuum glazing with small support pillars.

Infra-red thermography techniques may provide a potential method for in-service confirmation that the internal pressure remains sufficiently low to provide good thermal insulation. This method does not require high-accuracy measurements of the U-value: it is though, sensitive to the difference in air temperature either side of the enclosure and the air heat transfer coefficients, hence can only be used to compare a vacuum enclosure with a similar “specimen”. Further work is needed to develop this approach for assessing enclosures post-installation.

This research presents an accurate and reproducible fabrication method for a flat vacuum enclosure which has the potential to be exploited in flat vacuum solar collector technology.

Acknowledgements

The authors are grateful to the Engineering and Physical Sciences Research Council (EPSRC) for funding this work as part of a collaborative programme between the University of Warwick, Loughborough University and Ulster University, reference EP/K009915/1, EP/K010107/1 and EP/K009230/1.

References

Abbate, P., 2012. Presentation on the TVP Evacuated Panel at InterSolar 2012. < https://www.youtube.com/watch?v=z_4FD4Zxwew > (accessed 12/7/2017).
Arya, F., Hyde, T., Henshall, P., Eames, P., Moss, R., Shire, S., 2014. Fabrication and characterisation of slim flat vacuum panels suitable for solar applications. In: EuroSun2014, Aix-les-Bains, France, September 2014, pp. 505–511. http://proceedings.ises.org/paper/eurosun2014/eurosun2014-0045-Arya.pdf.
Arya, F., Hyde, T., Henshall, P., Eames, P., Moss, R., Shire, S., Zacharopoulos, A., 2015. Thermal analysis of flat evacuated glass enclosure for building integrated solar applications. 10th ENERGY FORUM Conference, Bern, Switzerland, Nov 2015.
Arya, F., 2014. Developing Alternative Sealing Materials in Fabrication of Evacuated Glazing at Low Temperature. Thesis (PhD). Ulster University.
Beikircher, T., Goldemund, G., Benz, N., 1996. Gas heat conduction in an evacuated tube solar collector. Sol. Energy 58 (4–6), 213–217.
Beikircher, T., Möckl, M., Osgyan, P., Streib, G., 2015. Advanced solar flat plate collectors with full area absorber, front side film and rear side vacuum super insulation. Sol. Energy Mater. Sol. Cells 141, 398–406.
Bellex datasheet, 2016. < http://www.bellexinternational.com/products/cerasolzer/ > (accessed 28.10.16).
Benvenuti, C., Ruzinov, V., 2010. The SRB evacuated flat solar panel. Proceedings of ECOS, 2010. p.2-429–434.
Benvenuti, C., 2013. The SRB solar thermal panel. Europhys. News 16–18. https://doi.org/10.1051/epn/2013301.
Benz, N., Beikircher, T., 1999. High efficiency evacuated flat-plate solar collector for process steam production. Sol. Energy 65, 111–118. https://doi.org/10.1016/S0038-092X(98)00122-4.
Benz, N., Beikircher, Th., Aghazadeh, B., 1996. Aerogel and krypton insulated evacuated flat-plate collector for process heat production. Sol. Energy 58 (1–3), 45–48.
British Standard BS 874: Part 3: Section 3.1: 1987, British standard methods for determining thermal insulating properties. Tests for thermal transmittance and conductance. Guarded hot-box method.
British Standards BS EN 675:2011 - Glass in building. Determination of thermal transmittance (U value) - Heat flow meter method.
British Standards BS EN ISO 8990: 1996, Thermal insulation. Determination of steady state thermal transmission properties. Calibrated and guarded hot box.
Buttinger, F., Beikircher, T., Pröll, M., Schölkopf, W., 2010. Development of a new flat stationary evacuated CPC-collector for process heat applications. Sol. Energy 84, 1166–1174.
Colangelo, G., Favale, E., Miglietta, P., de Risi, A., 2016. Innovation in flat solar thermal collectors: a review of the last ten years experimental results. Renew. Sustain. Energy Rev. 57, 1141–1159.
Collins, R.E., Simko, T.M., 1998. Current Status of the science and technology of vacuum glazing. Sol. Energy 62 (3), 189–213.
Collins, R.E., Turner, G.M., Fischer-Cripps, A.C., Tang, J.Z., Simko, T.M., Dey, C.J., Clugston, D.A., Zhang, Q.C., Garrison, J.D., 1995. Vacuum glazing – a new component for insulating windows. Build. Environ. 30 (4), 459–492.
Eames, P.C., 2008. Vacuum glazing: current performance and future prospects. Vacuum 82, 717–722. https://doi.org/10.1016/j.vacuum.2007.10.017.
Eaton, C.B., Blum, H.a., 1975. The use of moderate vacuum environments as a means of increasing the collection efficiencies and operating temperatures of flat-plate solar collectors. Sol. Energy 17, 151–158. https://doi.org/10.1016/0038-092X(75)90053-5.
Fang, Y., Eames, P.C., Norton, B., Hyde, T.J., 2006. Experimental validation of a numerical model for heat transfer in vacuum glazing. Sol. Energy 80, 564–577.
Fang, Y., Eames, P.C., Norton, B., 2007. Effect of glass thickness on the thermal performance of evacuated glazing. Sol. Energy 81, 395–404.
Fischer-Cripps, A.C., Collins, R.E., Turner, G.M., Bezzel, E., 1995. Stresses and fracture probability in evacuated glazing. Build. Environ. 30, 41–59. https://doi.org/10.1016/0360-1323(94)E0032-M.
Ganguli, A.A., Pandit, A.B., Joshi, J.B., 2009. CFD simulation of heat transfer in a two-dimensional vertical enclosure. Chem. Eng. Res. Des. 87, 711–727.
Ganguli, A.A., Pandit, A.B., Joshi, J.B., 2007. Numerical predictions of flow patterns due to natural convection in a vertical slot. Chem. Eng. Sci. 62 (16), 4479–4495.
Henshall, P., Eames, P., Arya, F., Hyde, T., Moss, R., Shire, S., 2016. Constant temperature induced stresses in evacuated enclosures for high performance flat plate solar thermal collectors. Sol. Energy 127, 250–261.
Henshall, P., Moss, R., Arya, F., Eames, P., Shire, S., Hyde, T., 2014. An evacuated enclosure design for solar thermal energy applications. Grand Renewable Energy Conference, July 2014, Tokyo, Japan. . http://proceedings.ises.org/paper/eurosun2014/eurosun2014-0039-Moss.pdf.
Hyde, T.J., Griffiths, P.W., Eames, P.C., Norton, B., 2000. Development of a novel low temperature edge seal for evacuated glazing. In: World Renewable Energy Congress VI, Brighton, UK. Pergamon, Oxford, pp. 271–274.
International Standard Organization, 1994. ISO 8990: 1994. Thermal insulation - Determination of steady-state thermal transmission properties - Calibrated and guarded hot box. Geneva, Switzerland.
JB Weld data sheet, 2014. Available online at < http://www.jb-weld.co.uk/images/technical-data-sheets/Epoxy_Putty_Stick_-_Steel_FINAL.pdf > .
Kennard, E.H., 1938. Kinetic Theory of Gases. McGraw-Hill International Book Company, New York.
Kim, Y.S., Balkoski, K., Jiang, L., Winston, R., 2013. Efficient stationary solar thermal collector systems operating at a medium-temperature range. Appl. Energy 111,

1071–1079.
Lewis, B.G., 1995. Sealing vacuum and cryogenic components with indium. CryoGas Int. 2–23.
Pilkington K-Glass Information Sheet. Pilkington Glass Limited, St. Helens, UK. https://www.pilkington.com/en-gb/uk/products/product-categories/thermal-insulation/pilkington-k-glass-range/pilkington-k-glass-a.
Moss, R.W., Shire, G.S.F., Henshall, P., Eames, P.C., Arya, F., Hyde, T., 2018a. Design and fabrication of a hydroformed absorber for an evacuated flat plate solar collector. Appl. Therm. Eng. Appl. Therm. Eng. 138, 456–464.
Moss, R.W., Shire, G.S.F., Henshall, P., Eames, P.C., Arya, F., Hyde, T., 2017. Optimal passage size for solar collector microchannel and tube-on-plate absorbers. Sol. Energy 153, 718–731.
Moss, R.W., Henshall, P., Arya, F., Shire, G.S.F., Eames, P.C., Hyde, T., 2018b. Simulator testing of evacuated flat plate solar collectors for industrial heat and building integration. Sol. Energy 164, 109–118.
Moss, R.W., Henshall, P., Arya, F., Shire, G.S.F., Hyde, T., Eames, P.C., 2018c. Performance and operational effectiveness of evacuated flat plate solar collectors compared with conventional thermal, PVT and PV panels. Appl. Energy 216, 588–601.
Sgobba, S., 2006. Materials for High Vacuum Technology: An Overview. No. CERN-TS-2006-004. CERN, pp. 117–144. https://doi.org/10.5170/CERN-2007-003.117.
Zhao, J.F., Eames, P.C., Hyde, T.J., Fang, Y., Wang, J.A., 2007. Modified pump-out technique used for fabrication of low temperature metal sealed vacuum glazing. Sol. Energy 81, 1072–1077.